applied sciences

MDPI

Article

Bridge-Borne Noise Induced by High-Speed Freight Electric Multiple Units: Characteristics, Mechanisms and Control Measures

Miao Du [1], Kaiyun Wang [1,2], Xin Ge [3] and Xiaoan Zhang [1,*]

[1] School of Mechanical Engineering, Lanzhou Jiaotong University, Lanzhou 730070, China; dumiao01@foxmail.com (M.D.); kywang@swjtu.edu.cn (K.W.)
[2] State Key Laboratory of Rail Transit Vehicle System, Southwest Jiaotong University, Chengdu 610031, China
[3] CRRC Qingdao Sifang Co., Ltd., Qingdao 266111, China; gexin19940428@foxmail.com
* Correspondence: zxa_lzjtu@163.com

Abstract: The high-speed freight electric multiple unit (EMU) is one of the important development directions for railway freight transportation. To investigate the bridge radiation noise induced by the freight EMU, a noise prediction model consisting of the containers–vehicle–track–bridge dynamic model, finite element model, and boundary element model are established and validated. Through simulation, the bridge radiation noise under different train loading conditions is compared, and the noise radiation mechanism is revealed. Moreover, the noise reduction effect of the noise wall is studied, and the influences of noise wall heights and sound absorption materials are investigated. Results indicate that the bridge sound power and the sound pressure levels (SPLs) of near-field points increase slightly with train loads in the frequency range below 20 Hz and above 125 Hz, with a maximum increase of about 6.8 dB. The structure resonance, intense local vibration, and high acoustic radiation efficiency cause strong bridge radiation noise. The noise wall can realize a good overall noise reduction effect in the sound shadow zone; nevertheless, SPLs increased in areas between the bridge and the noise wall. The ground reflection affects the superposition of transmitted, reflected, and diffracted sound waves, which causes nonlinear relationships of noise reduction effects with the noise wall height. From the perspective of human hearing sensitivity, the loudness levels of typical field points increase with the frequency in the range of 20~80 Hz, and SPLs below 25 Hz are less than the threshold of hearing. Setting the noise wall can effectively reduce the loudness levels, and the reduction effect increases with the noise wall height.

Keywords: noise prediction model; bridge radiation noise simulation; sound pressure level; noise wall

Citation: Du, M.; Wang, K.; Ge, X.; Zhang, X. Bridge-Borne Noise Induced by High-Speed Freight Electric Multiple Units: Characteristics, Mechanisms and Control Measures. *Appl. Sci.* **2024**, *14*, 2801. https://doi.org/10.3390/app14072801

Academic Editor: Gino Iannace

Received: 21 February 2024
Revised: 18 March 2024
Accepted: 24 March 2024
Published: 27 March 2024

1. Introduction

High-speed railway is one of the important land transportation modes, which greatly promotes regional economic development. In the recent few decades, China has established the largest high-speed railway network in the world. The operating mileage of high-speed railways in China has achieved 45,000 km, which accounts for over 70% of the global total [1]. To explore the transportation potential of existing high-speed railway lines, a new type of freight electric multiple unit (EMU) at speeds above 250 km/h was developed to fill the gap in fast freight transportation. Bridges are widely adopted to accommodate the need for a smooth and high-speed operation of high-speed trains, but the structure-borne noise of bridges induced by trains may have an adverse impact on the ecological environment along the line [2]. Therefore, it is of great significance to conduct research on bridge-borne noise, which can provide a reference for the future operation of freight EMU trains.

In the early stages of bridge-borne noise research, studies mainly emphasized the experiments of acoustic characters. Moritoh et al. [3] measured the structure-borne noise of concrete bridges induced by high-speed trains on the Shinkansen, and the sound pressure of the measuring point beneath the bridge was revealed to be dominant at 100 Hz. Ngai et al. [4] conducted vibration and noise tests on a concrete viaduct bridge in Hong Kong, indicating that the main frequency range of bridge vibration and noise is 20~157 Hz. Poisson et al. [5] conducted noise tests on a single-line simply supported steel truss bridge with a span of 20.8 m and the roadbed section. Compared with the results of the roadbed section, the noise generated by trains passing over the steel bridge was 10~14 dB(A) higher. Liang et al. [6] studied the vibro-acoustic characteristics of a large-span plate-truss composite bridge in urban rail transit. The wheelsets' periodic excitation and wheel–rail irregularity were revealed to affect the bridge response, and the rail and slab are decoupled beyond the natural frequency of the rail-fastener system. With computer technology advancing, simulation methods were introduced to bridge radiation noise studies. Zhang et al. [7,8] analyzed the bridge radiation noise in the low-frequency range based on a detailed train–track–bridge dynamic model, which is revealed to be affected by resonance characteristics, modal acoustical radiation efficiency, and severe vibration. Li et al. [9] studied the structure-borne noise characteristics of a steel-concrete bridge with a statistical energy analysis (SEA)-based model and field tests, and the results indicated that the noise from the web of steel longitudinal girder was dominant in the frequency range above 315 Hz, and the corresponding frequency range for the concrete deck was between 80 and 160 Hz. Li et al. [10] proposed a general procedure for predicting the low-frequency concrete bridge-bone noise in the time domain, in which the frequency-dependent modal acoustic transfer vectors were determined using the boundary element method (BEM), and the sound pressures were obtained with time-frequency transforms. The procedure was validated with the measured data of a U-shaped concrete bridge. Based on this, Li et al. [11] further proposed a 2.5-dimensional method with the combination of the two-dimensional BEM and space-wave number transforms, and the simulation results in the near field agreed well with measured data. Song et al. [12] compared the noise characteristics of single-span and multi-span bridges using the 2.5-dimensional method; the results indicated that the single-span bridge model could meet the demand of noise prediction in the near field, but the multi-span bridge model must be considered for the analysis in the far field, and the suggested length of the bridge model was about twice the distance between the track center and the interested field point.

To mitigate bridge-borne noise, many vibration and noise reduction measures were implemented and studied. Wu et al. [13] tested the structural noise on the box girder and U-shaped girder sections of the Shanghai rail transit line, finding that the A-weighted sound pressure level (SPL) in the U-shaped girder section was 2.5 dB lower than that in the box girder section. Liu et al. [14] conducted vibration and noise tests on a 30 m U-shaped girder bridge equipped with vibration-damping fasteners and found that the fasteners can effectively reduce the vibration but have little effect on acoustic control. Zbiciak et.al [15,16] carried out tests under slab mats to reduce under-rail vibrations; they found that slab mats can effectively reduce vibrations in the frequency range above 34 Hz, and the insertion loss for the 30 mm thickness of under slab mats is up to 75%. Wettschureck et al. [17,18] conducted field tests on the railway line installed under ballast mats. The under-ballast mats were proved to be effective in reducing structural vibration, and the service life of which attains at least 30 years. Ahac et al. [19] compared the vibration characteristics of tracks with or without sleeper mats with tests, and under-sleeper mats were revealed to reduce track vibration by 30%. Liang et al. [20] studied the vibration and noise of a long-span steel truss cable-stayed bridge laid with damping pads, and the bridge noise was tested to reduce noise by 10~13 dB(A). Li et al. [21] compared the radiation noise of U-shaped, single-box, and double-box girder bridges, and the radiation noise of the single and double box-girder bridges was 8.6 and 11.7 dB lower than that of the U-shaped beam bridge. Harrison et al. [22] studied panel acoustic contributions of a steel-concrete bridge with a SEA model considering the roughness of the wheel–rail interface, and the noise reduction measure by optimizing the bridge structure was proposed. Zhang et al. [23,24]

investigated the train-induced noise of a box-girder bridge using an integrated FEM-BEM method and further studied the noise reduction effects of increasing the thickness of the deck, adjusting the inclination of webs to 0~12°, strengthening the boundary constraints, and adding a longitudinal clapboard.

Many scholars have conducted research on the structure-borne noise of railway bridges, but studies involving the noise induced by high-speed freight EMUs are seldom, and so is the research on the acoustic control measures from the perspective of the transmission path. Therefore, the radiation noise of a 32 m concrete simply supported box girder induced by a high-speed freight EMU is investigated. Considering the coupled vibration relationship between the car body and containers, a bridge-borne noise prediction model composed of a coupled vehicle–track–bridge dynamics model, a track–bridge finite element model, and a bridge acoustic boundary element model was established. The acoustic characteristics and the panel contributions of the bridge radiation noise under empty and loaded container conditions are compared, and the mechanism of the bridge-borne noise is analyzed. Moreover, the noise reduction effect of the noise wall as well as the influence of wall heights is studied. The analysis results indicate that the main frequency of the bridge acoustic power is around 71 Hz, and the structure resonance is the main cause of the noise peak. Setting noise walls can effectively reduce the noise behind the wall, especially in the sound shadow zone.

2. The Bridge-Borne Noise Prediction Model

The bridge-borne noise prediction model consists of the vehicle–track–bridge coupled dynamic model, the track–bridge finite element model, and the bridge boundary element model, as shown in Figure 1. The dynamic model is used to compute the wheel–rail interaction forces excited by irregularities. The time-domain wheel–rail force is further used as the input of the track–bridge finite element model to solve the vibration responses of the track–bridge system. Finally, the bridge vibration responses are imported into the bridge acoustic boundary model as the acoustic boundary condition to calculate the bridge radiated noise.

2.1. The Vehicle–Track–Bridge Coupled Dynamics Model

The vehicle–track–bridge coupled dynamics model consists of three subsystems: the freight EMU vehicle, the ballastless slab track, and the bridge. In the vehicle model, each car body of the EMU comprises 20 containers with the size of 1.5 m × 1.35 m × 2 m, and the dead load and carrying capacity of each container are 210 kg and 850 kg. The containers are symmetrically arranged along the centerline of the car body, and containers are mounted to the car body floor via a series of restraining wedges integrating elastomers. The car body, containers, bogie frames, and wheelsets are modeled as rigid bodies, and each of them has six degrees of freedom (DOFs), namely the longitudinal, lateral, vertical, roll, yaw, and pitch motions, which form a 162 DOFs multi-body system. The restraining wedges between containers and the car body are simplified as force elements with three-dimensional stiffness. The primary and secondary suspension systems are modeled as spring–damper elements, in which the air spring provides three-dimensional stiffness and damping, and the anti-hunting damper as well as the lateral and vertical dampers provide appropriate damping.

For the ballastless slab track, the rails are modeled as simply supported Timoshenko beams considering the vertical, lateral, and torsional motions. The track slabs are described as elastic rectangle plates supported on a viscoelastic foundation, in which only the rigid mode of the slab lateral vibration is considered [25]. The fastenings and rail pads are simplified as discrete spring–damper elements, and the cement asphalt (CA) mortar layer is simulated by uniformly distributed stiffness and damping. The bridge dynamics model is established based on a FEM model, which is introduced in the subsequent chapter in detail. The modal analysis is conducted to obtain the modal frequencies as well as the full mass and stiffness matrices of the bridge, and Rayleigh damping is adopted to describe the damping characteristic of the bridge. The interaction between the track and bridge is discretized as a serial of point-to-point interaction modeled with linear spring–damper elements.

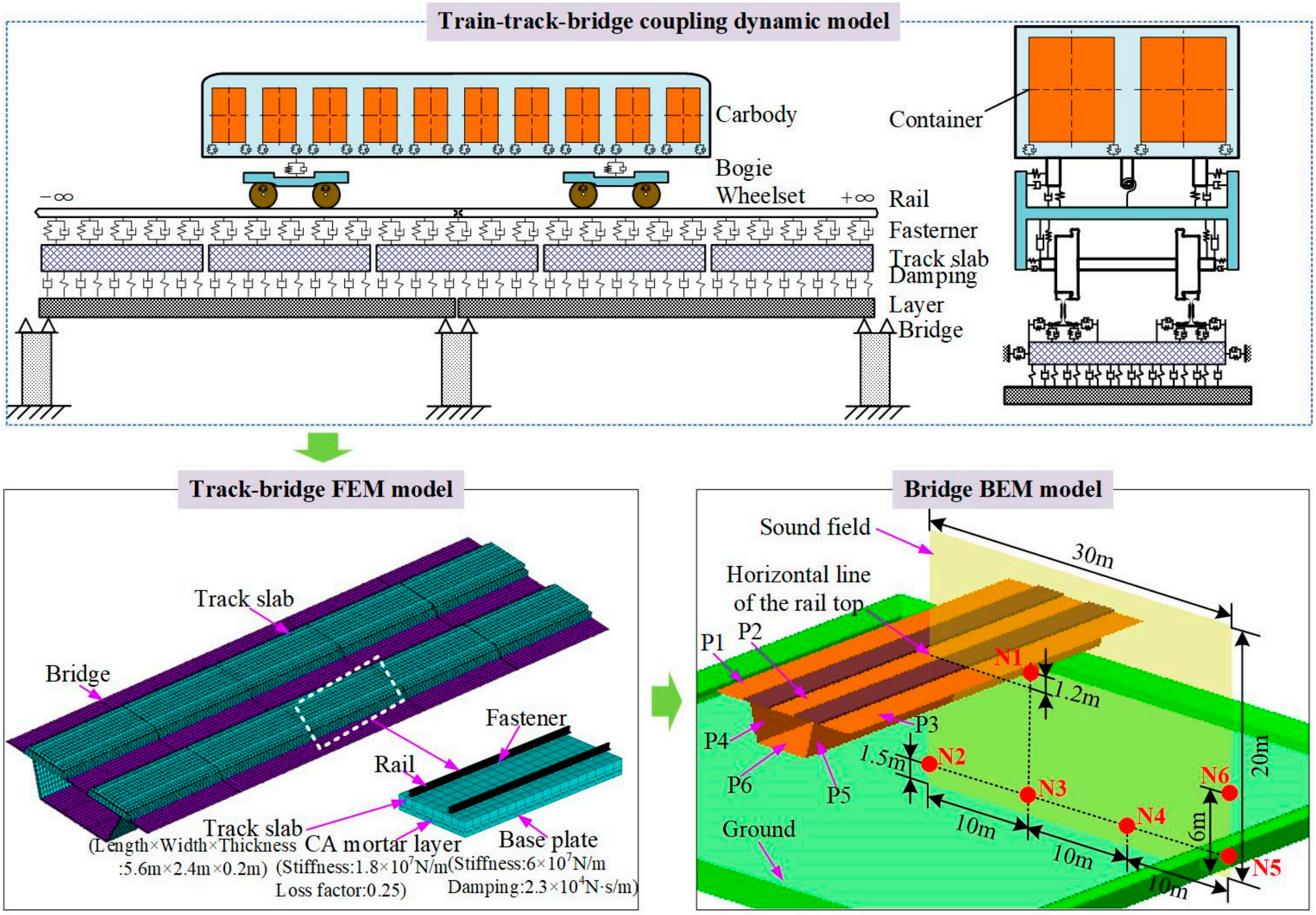

Figure 1. The prediction model of bridge-borne noise.

The dynamic equilibrium equations of the whole system can be expressed as

$$\begin{cases} M_c\ddot{x}_c + C_c\dot{x}_c + K_c x_c = F_c \\ M_v\ddot{x}_v + C_v\dot{x}_v + K_v x_v = F_v - F_c \\ M_t\ddot{x}_t + C_t\dot{x}_t + K_t x_t = F_t - F_v \\ M_b\ddot{x}_b + C_b\dot{x}_b + K_b x_b = F_b \end{cases} \tag{1}$$

where M, C, and K denote the mass, damping, and stiffness matrixes, respectively; $\ddot{x}$, $\dot{x}$, and x are the acceleration (m/s^2), velocity (m/s), and displacement (m) vectors, respectively; F denotes the force vector (N); subscripts c, v, t, and b represent the container, vehicle, track, and bridge, respectively. For the wheel–rail interaction, the normal forces are determined based on the nonlinear Hertz contact theory as

$$F_n(t) = \begin{cases} \left[\frac{1}{G}Z_{wr}(t)\right]^{3/2}, & Z_{wr}(t) > 0 \\ 0, & Z_{wr}(t) \le 0 \end{cases} \tag{2}$$

where G denotes the wheel–rail contact constant; $Z_{wr}(t)$ denotes the elastic compressing amount at the wheel–rail contact point. The wheel–rail creep forces are calculated using the FASTSIM algorithm developed by Kalker [26]. The main parameters of the train are listed in Table 1.

Table 1. Key parameters of the freight EMU.

Parameters		Value	Unit
Mass of the car body		33,660	kg
Mass of the container (dead load/carrying capacity)		210/850	kg
Mass of the bogie frame		2235	kg
Mass of the wheelset		1451	kg
Primary suspension stiffness (each side)	Longitudinal	9.2×10^5	$N{\cdot}m^{-1}$
	Lateral	9.2×10^5	$N{\cdot}m^{-1}$
	Vertical	7.5×10^5	$N{\cdot}m^{-1}$
Stiffness of the axle box rubber joint	Longitudinal	4×10^7	$N{\cdot}m^{-1}$
	Lateral	1.2×10^7	$N{\cdot}m^{-1}$
Secondary suspension stiffness (unloaded/loaded)	Longitudinal	$1.13 \times 10^5/1.23 \times 10^5$	$N{\cdot}m^{-1}$
	Lateral	$1.13 \times 10^5/1.23 \times 10^5$	$N{\cdot}m^{-1}$
	Vertical	$1.85 \times 10^5/2.15 \times 10^5$	$N{\cdot}m^{-1}$
Equivalent three-dimensional stiffness of the restraining wedge		1×10^7	$N{\cdot}m^{-1}$

In the simulation, the ballastless track spectrum of the Chinese high-speed railway superimposed with a measured shortwave spectrum is adopted for track excitations. A mixed explicit–implicit integration method based on the Zhai method and the Newmark-β method is employed to solve the dynamic response of the train–track–bridge system.

2.2. The Track–Bridge FEM Model

The bridge employed for this study is a standard double-line concrete box girder widely used in Chinese high-speed railways, and the track structure on the bridge adopts the CRTS II-type ballastless slab, which is composed of rail, fastenings, track slabs, CA mortar layer, and base plate. The rail profile is CHN 60 kg/m. The bridge span is 32.6 m, and the widths of the deck and the bottom flange are 13.4 m and 4.8 m, respectively. The thicknesses of the deck, bottom flange, and webs are 315 mm, 480 mm, and 300 mm, respectively, and the simulated rails are (40 + 32.6 + 40) m long. The track–bridge FEM model is developed using the software ANSYS 19.0, as shown in Figure 1. The rails are modeled with beam188 elements, and the track slab and base plate are modeled with Solid45 elements. The Combin14 spring elements are adopted for modeling the fastening/rail pad system and the CA mortar layer. The bridge is modeled as four thin plates using Shell181 elements, and the Rayleigh damping is used to deal with the damping of the bridge.

2.3. The Bridge BEM Model

In the acoustic boundary element theory, the sound pressure of the analysis area Ω in the ideal medium obeys the wave equation [27,28].

$$\nabla^2 P(s,t) = \frac{1}{c^2}\frac{\partial^2 p(s,t)}{\partial t^2} \tag{3}$$

where ∇^2 is the Laplace operator; $P(s,t)$ is the sound pressure (Pa) of point s at time t (s); c is the sound speed (m/s). Considering the independence of time, the sound pressure of a harmonic sound field can be expressed as

$$P(s,t) = p(s)\mathrm{e}^{-i\omega t} \tag{4}$$

where i is the imaginary unit; ω is the angular frequency (rad/s). Substituting Equation (4) into Equation (3) yields the sound pressure-based Helmholtz control differential equation:

$$\nabla^2 p(s) + k^2 p(s) = 0 \tag{5}$$

where k represents the wave number of the sound wave.

For acoustic problems in general bounded spaces without distributed source terms, Equation (5) has the following Helmholtz solution, which represents the sound pressure of the point s in the sound field, with the integral form of [8], as follows

$$p(s) = \begin{cases} \int_\Gamma \begin{bmatrix} G(s,y)q(y)- \\ \frac{\partial G(s,y)}{\partial n(y)} p(y) \end{bmatrix} d\Gamma(y), s \in \Omega, s \notin \Gamma \\ \frac{1}{c(s)} \int_\Gamma \begin{bmatrix} G(s,y)q(y) \\ -\frac{\partial G(s,y)}{\partial n(y)} p(y) \end{bmatrix} d\Gamma(y), s \in \Gamma \end{cases} \tag{6}$$

where Green's function $G(s,y) = \frac{e^{ikR(s,y)}}{4\pi R(s,y)}$ represents the sound pressure at point s produced by a point sound source with unit intensity located at point y in the space; Γ is the surface boundary of the sound source, n represents the outward normal direction on the surface boundary of the sound source; $c(s)$ is the coefficient related to the geometric characteristics of point s. Discretizing Equation (6) using the boundary element method, the structure radiated acoustic power (W) can be obtained as [27], as follows:

$$W = -\frac{1}{2}\mathrm{Re}\left\{ \int_\Gamma P_\Gamma(s) v_\Gamma(s)^* d\Gamma(s) \right\} \tag{7}$$

where Re denotes the real part of a complex number; superscript * represents complex conjugation; $v_\Gamma(s)$ denotes the normal velocity at point s.

Taking the above vibration responses of the FEM mode as the boundary condition, the BEM model of a box girder bridge is established in the software Virtual. Lab 13.6. The mesh size is required to be less than 1/6 of the shortest wavelength of the analysis frequency. As the maximum analysis frequency analyzed in this study is 200 Hz, the maximum mesh size is determined as 0.28 m, and the mesh size of 0.2 m is adopted in the modeling. A sound field with the size of 20 m $\times$ 30 m is established at the middle cross-section of the bridge span, and the ground is considered as a total reflecting surface.

2.4. Model Validation

To ensure the accuracy of the simulation results, it is necessary to validate the model. As the freight EMU train has not been placed into official operation, relevant experiments cannot be carried out. Therefore, the tested results under the condition of a high-speed passenger train passing through a bridge are adopted to verify the model. It should be noted that the bridge and track types at the test site are consistent with those in the model, the same operating conditions are set in the simulation, and the train speed is about 220 km/h. The test content includes the bridge bottom plate acceleration and the bridge radiated noise near the deck, as shown in Figure 2a. The acceleration sensor used in the test is INV9824 with a measurement range of 1000 g (produced by COINV, Beijing, China), and the INV9206 noise sensor (produced by COINV, Beijing, China) is adopted to measure noise from 20 dB to 146 dB. The data acquisition system adopted a 16-channel device by the IMC GmbH. Figure 2b,c show the comparisons of measured and computed bridge accelerations in the time and frequency domains, respectively.

It can be observed that the vibration amplitudes of computed results in the time domain are consistent with the measured one, and both the main frequencies of the measured and computed acceleration RMS are around 50 Hz with close amplitudes. Figure 2d shows the comparison of the measured and computed 1/3 octave band SPLs at the test point. It can be seen that both the main frequencies of measured and computed SPLs are 50 Hz, and the overall trends of the SPLs in the frequency range of 20~200 Hz are similar; correspondingly, the SPLs are close. In summary, the computed results are in good agreement with those of the tested results, which verifies the effectiveness of the simulation model.

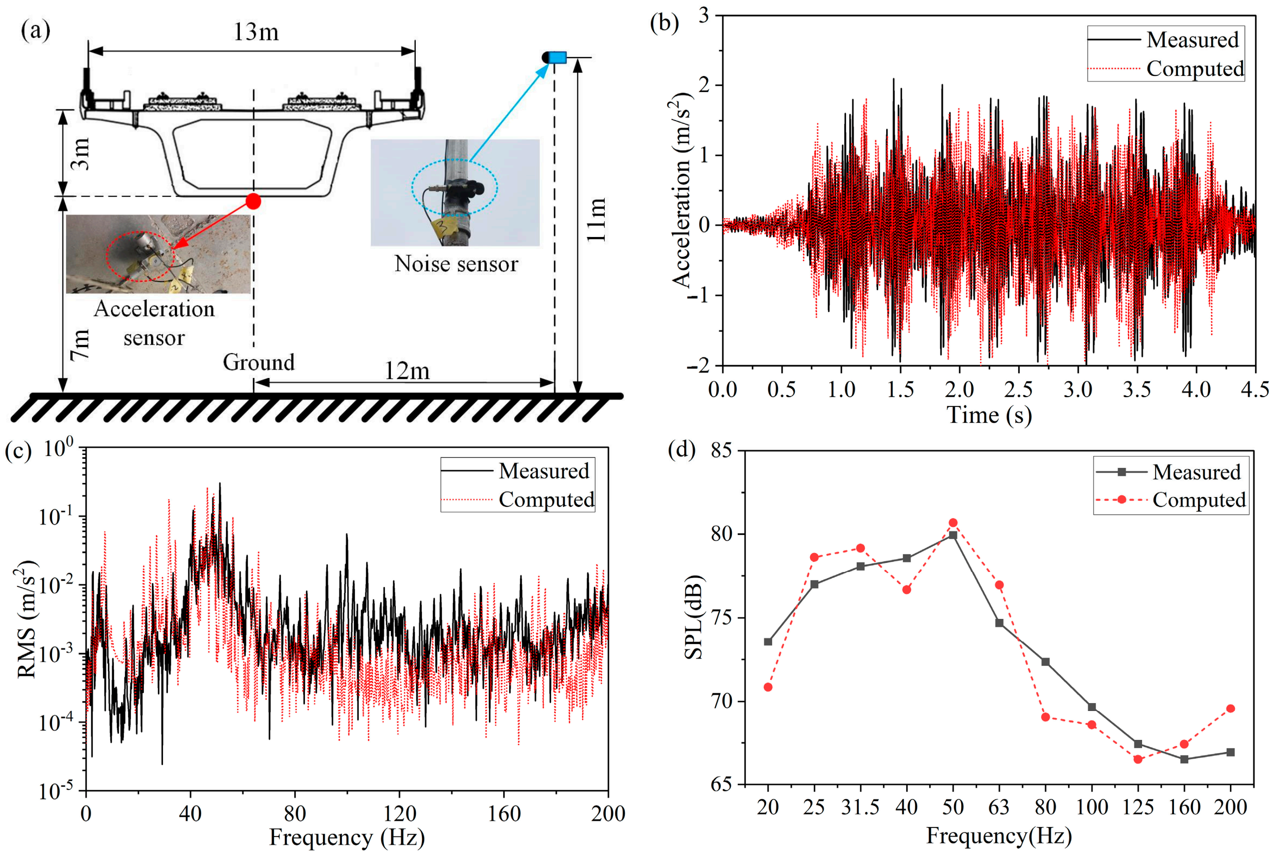

Figure 2. Model validation results: (**a**) arrangement of test points; (**b**) comparison of bridge acceleration in the time domain; (**c**) comparison of bridge acceleration RMS in the frequency domain; (**d**) comparison of 1/3 octave band SPLs.

3. Characteristics and Mechanisms of Bridge Vibration and Structure-Borne Noise

Based on the above bridge-borne noise prediction model, the characteristics of bridge vibration and radiation noise under different load conditions are analyzed. The panel contributions to typical field points are studied, and the mechanism of bridge radiated noise is discussed from the perspectives of bridge mode shape, vibration cloud, and sound radiation efficiency.

3.1. Characteristics of Bridge Vibration and Radiated Noise

Taking the condition of the freight EMU passing through the bridge at 350 km/h as an example, the characteristics of wheel–rail forces, bridge vibration, and bridge radiation noise under conditions of empty and loaded containers are analyzed. Figure 3a shows the comparison of vertical wheel–rail forces in the time domain. It can be seen that the wheel–rail forces under a loaded containers condition are significantly larger than that of an empty containers condition, and the wheel–rail forces of the two conditions fluctuate around 68 kN and 88 kN, respectively, but the corresponding fluctuation ranges are close. Figure 3b shows the comparison of acceleration in the frequency domain at the center position of the deck. It can be seen that the overall trends of accelerations under two conditions are consistent in the range below 200 Hz with main frequencies of 71.2 Hz, in which the accelerations of loaded containers condition at frequency ranges below 15 Hz and above 165 Hz, and at frequencies such as 60.8 Hz, 92.0 Hz, and 137.2 Hz, they are slightly larger than that of empty containers condition, with a maximum difference of about 0.06 m/s^2.

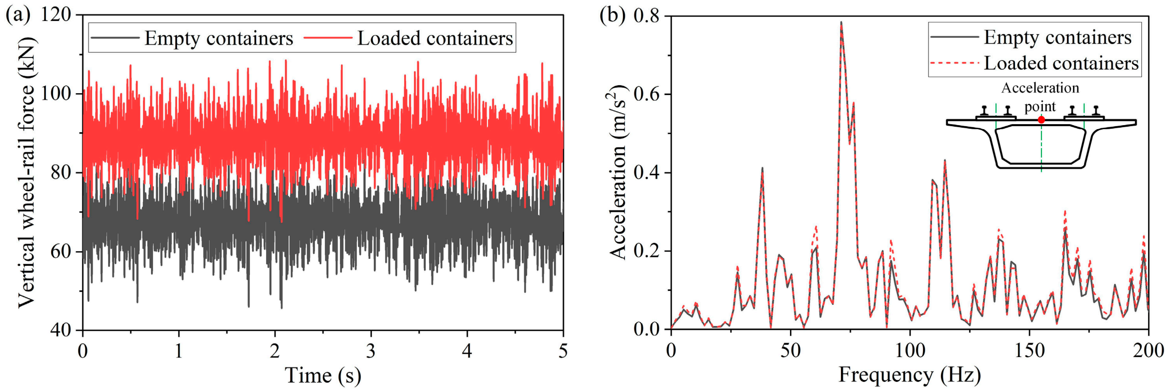

Figure 3. Dynamic responses of the vehicle–track–bridge system under different load conditions: (**a**) vertical wheel–rail forces; (**b**) bridge deck accelerations.

Figure 4 shows the comparison of bridge acoustic powers under two load conditions. Similar to the bridge vibration results, the acoustic powers of the two conditions are close with the same main frequencies of 71 Hz, and both the maximum acoustic powers are around 125.9 dB. The main frequencies of simulated acoustic power are consistent with that in Ref. [29]. In the frequency range below 40 Hz and above 120 Hz, the bridge acoustic power of the loaded containers condition is slightly larger than that of the empty containers condition, and the maximum increase is about 2.4 dB.

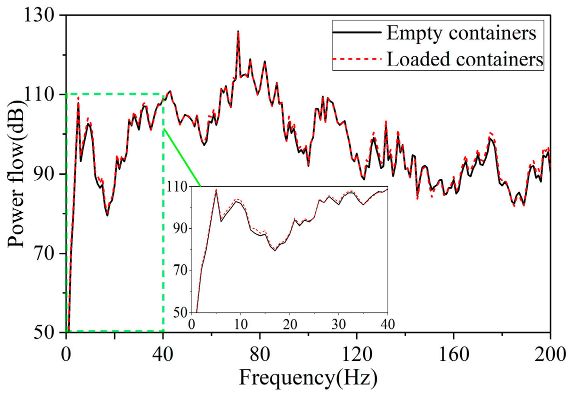

Figure 4. Comparison of bridge acoustic powers under different load conditions.

Moreover, the standard noise test point N1 (1.2 m above the rail and 7.5 m away from the center of the near-track rail line [30]) and field points N2~N6 in Figure 1 are selected as typical field points, and the characteristics of field point SPLs under two load conditions are compared, as shown in Figure 5. It can be seen that the SPLs of the two load conditions are consistent at the same field point, and the main frequencies of SPLs at points N1~N6 are at 80 Hz with the maximum SPL around 83~88 dB. The prominent differences between the SPLs under the two conditions lie in the frequency range of 20 Hz and below, in which the SPLs under the loaded containers condition are larger than that of the empty containers condition, and the maximum difference is about 2 dB. In addition, the SPLs under loaded container conditions are also slightly larger than those under empty container conditions at the frequency range above 125 Hz.

To further study the panel contribution of the bridge to the above field points, taking the loaded containers condition as an example, Figure 6 shows contributions of the left flange plate (P1), deck (P2), right flange plate (P3), left web plate (P4), right web plate (P5), and bottom plate (P6) to the SPLs of each field point. As shown in Figure 6a, the main frequency of SPLs at the field point N1 is around 65~90 Hz, in which the deck, right flange plate, right web plate, and bottom plate contribute most to the SPLs. The prominent SPLs at the field point N2 are concentrated in the frequency ranges of 2~10 Hz and 65~90 Hz, and the main contribution plates are the deck and bottom plate, as shown in Figure 6b. For the field point N3, the contributions of the deck and bottom plate are relatively large in the frequency range of 2~10 Hz, and the bottom plate contributes significantly in the frequency range of 25~55 Hz, while the left and right flange plates and deck contribute most in the frequency range of 65~90 Hz (see Figure 6c). It can be seen from Figure 6d–f that the main frequencies of the SPLs at field points N4~N6 field points are around 65~90 Hz, and the right flange plate is the main contribution plate.

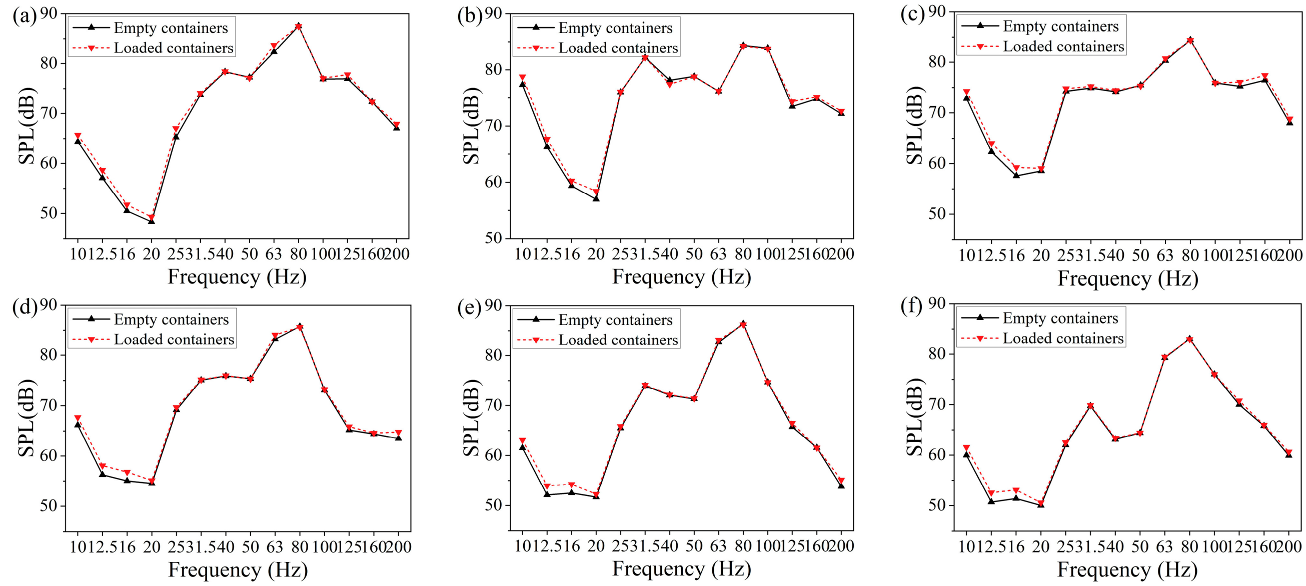

Figure 5. Comparisons of 1/3 octave band SPLs under different loading conditions at field points (**a**) N1; (**b**) N2; (**c**) N3; (**d**) N4; (**e**) N5; and (**f**) N6.

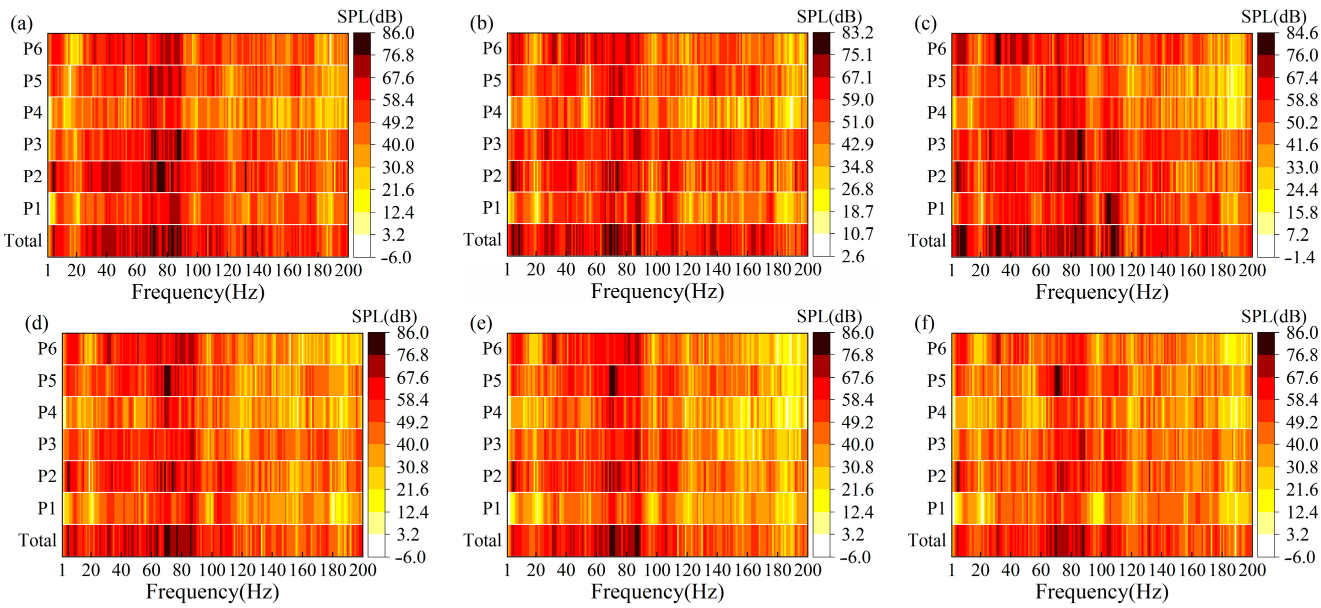

Figure 6. The panels' sound pressure contributions under the loaded containers condition at field points (**a**) N1; (**b**) N2; (**c**) N3; (**d**) N4; (**e**) N5; and (**f**) N6.

3.2. Mechanism Analysis of Bridge Radiated Noise

Based on the above analysis, the mechanism of bridge radiated noise is further investigated in this section. Figure 7 shows the bridge modal shapes and vibration clouds at peak frequencies of the bridge acoustic power, namely 43 Hz, 71 Hz, and 106 Hz. It can be seen that the bridge modal shape at 43.0 Hz presents local vibration of the deck and the bottom plate distributed along the centerline of plates, and there are six and three longitudinal bending half-waves on the deck and the bottom plate, respectively. By comparing the vibration cloud and modal shape around 43 Hz, it can be observed that the deck of the bridge resonates significantly induced by wheel loads, with a maximum acceleration of about 0.56 m/s^2. At the frequency of 70.1 Hz, the bridge modal shape mainly exhibits the local vibration of the deck near the center line, and six longitudinal and two lateral bending half-waves appear. The vibration cloud at 71.2 Hz presents intense local vibration near the center of the deck, and the maximum acceleration attains 2.06 m/s^2. Moreover, prominent local vibration at the bottom plate and the left and right flange plates can be observed, which is larger than that of the deck at 43 Hz. The bridge modal shape at 105.5 Hz is similar to that at 70.1 Hz, but the high-frequency vibration is more significant at 105.5 Hz due to the higher modal order, with eleven longitudinal and two lateral bending half-waves. The vibration cloud at 105.9 Hz appears several intense vibration zones overlapped with the local vibration area of the modal shape in the deck. The maximum acceleration is about 0.42 m/s^2, which is much smaller than that at 71.2 Hz. Li et al. [31] indicate that the local resonance of structures is one of the main causes of bridge radiation noise. The maximum local vibration of the deck at 71.2 Hz corresponds to the maximum bridge acoustic power at 71 Hz, and the maximum acceleration of the deck at 43.4 Hz is slightly larger than that at 105.9 Hz, but the local vibrations of the left and right web plates at 105.9 Hz is more intense, leading to the close acoustic powers at these two frequencies, which exactly coincides with the acoustic power results at peak frequencies in Figure 4.

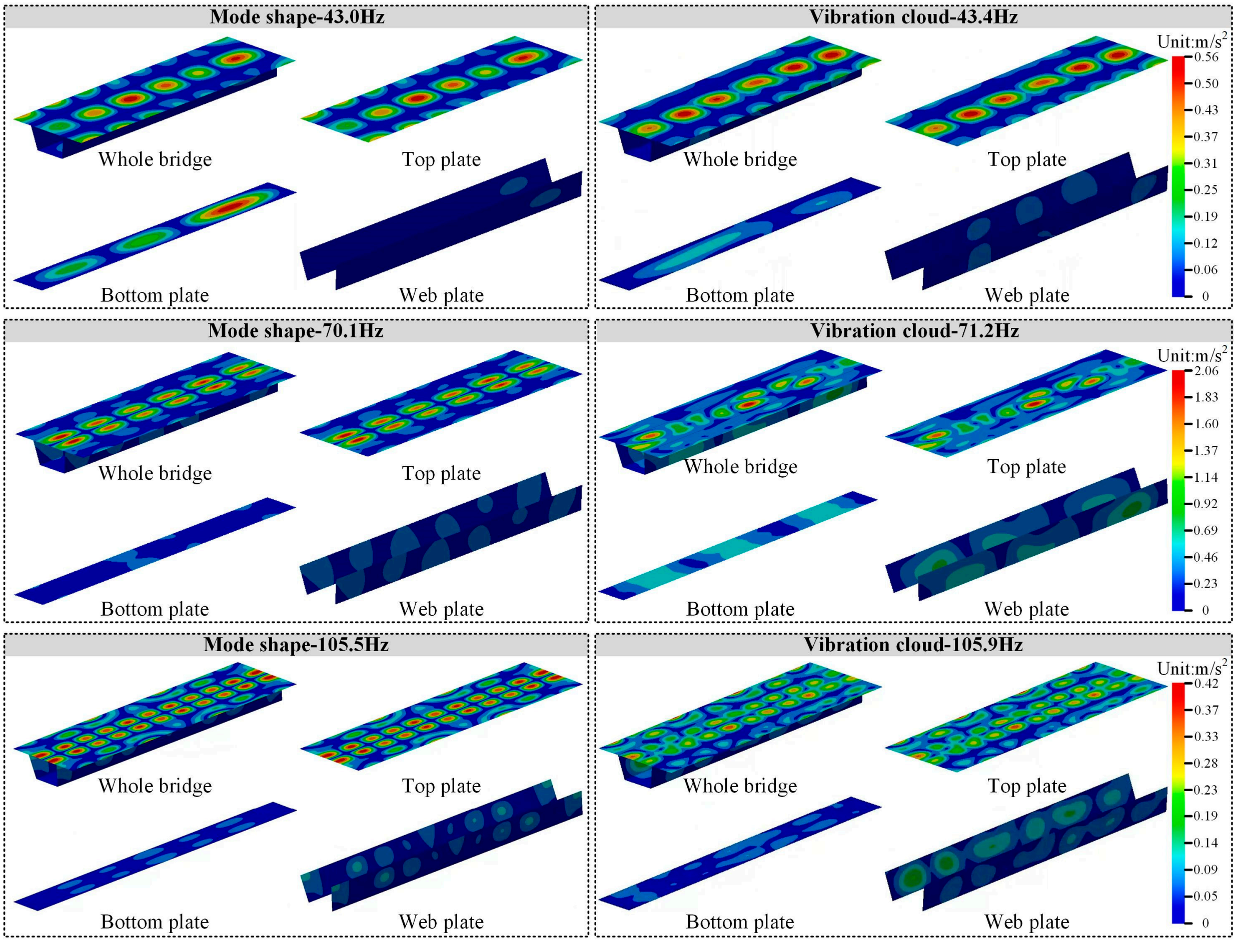

Figure 7. Characteristics of the bridge vibrations near peak frequencies of the acoustic power.

Figure 8 shows the acoustic radiation efficiency of the bridge in the frequency range of 0~200 Hz. It can be seen that there exist obvious peaks of the acoustic radiation efficiency at 71 Hz and 106 Hz, while the corresponding value at 43 Hz is relatively small. By combining the bridge acoustic power in Figure 4, it can be analyzed that both the maximum acoustic power and acoustic radiation efficiency lead to maximum SPLs around 71 Hz. The bridge acoustic powers around 105 Hz are close to that of around 43 Hz, but the larger acoustic radiation efficiency causes greater SPLs around 105 Hz.

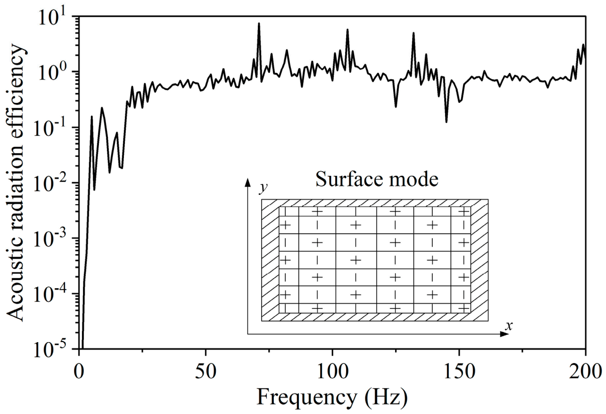

Figure 8. The bridge acoustic radiation efficiency.

The bridge is generally considered as multiple rectangular thin plates with different thicknesses in the research of bridge radiated noise, and the ideal thin plate theory is introduced to study the characteristics of acoustic radiation efficiency. Based on the acoustic radiation theory of bending waves in a finite plate, the critical frequency of the plate is [32,33] as follows:

$$f_c = c^2\sqrt{12\rho(1-\sigma^2)/E}/2\pi h \tag{8}$$

where ρ is the density of the plate; σ is Poisson's ratio; E is Young's modulus; h is the height of the plate. When the structural vibration frequency is less than the critical frequency of the plate, the plate radiates little energy to the far field, whilst when the structural vibration frequency is greater than or equal to the critical frequency, the plate has strong energy radiation ability. Moreover, the acoustic radiation efficiency of the plate can be determined by the relationship of acoustic wavenumbers and modal wavenumbers in the x and y directions, and the acoustic and modal wavenumbers can be calculated with

$$\begin{cases} k = \omega/c \\ k_x = m\pi/a \\ k_y = n\pi/b \end{cases} \tag{9}$$

where ω is the angular frequency, $\omega = 2\pi f$; c is the sound speed; f is the frequency; m and n are the longitudinal and lateral orders of modes, respectively. When $k_x < k < k_y$ (or $k_y < k < k_x$), the vibration radiation in the y-direction (or x-direction) is canceled out, and the acoustic waves are radiated in x-direction (or y-direction), known as the x-edge (or y-edge) mode; when $k_x > k$ and $k_y > k$, known as the corner mode, the radiation efficiency is lower than that of edge modes; when $k_x < k$ and $k_y < k$, known as the surface mode (the "+" and "−" represent different vibration directions of phase elements, as shown in Figure 8), which contains both x and y edges, and has a higher radiation efficiency than the other modes.

According to the above modal results of the bridge, the vibrations of the deck are dominant. The critical frequency of the plate with the same size as the deck is 53.4 Hz, and the corresponding k_x, k_y, and k at peak frequencies are listed in Table 2. As the frequency of 43 Hz is less than the critical frequency, the corresponding radiation efficiency is lower. For frequencies of 70.1 Hz and 105.5 Hz exceeding the critical frequency, the wavenumber components in both x and y directions are conformed to the surface mode. Thus, the deck has high acoustic radiation efficiencies at these two frequencies.

Table 2. Acoustic and modal wavenumbers of the deck at peak frequencies.

Frequency (Hz)	k	k_x	k_y
43.0	0.79	0.57	0.23
70.1	1.30	0.57	0.47
105.5	1.95	0.96	0.47

4. Noise Reduction Analysis of the Noise Wall

The control of bridge-borne noise is mainly implemented from the perspectives of noise source and noise transmission path. Noise reduction measures from the aspect of the sound source usually involve structural optimization or improvement, which is difficult to implement for completed bridges. Measures from the transmission paths' aspect are relatively flexible, which can effectively realize noise control in special sections and are widely used in urban transportation, and setting noise walls is the most common measure. Therefore, the effect of noise walls on reducing bridge-borne noise is analyzed in this chapter.

4.1. Noise Reduction Effect of the Noise Wall

Referring to an application case of the noise wall in a rail transit [34], the noise wall is set 10 m from the centerline of the bridge, and the wall height is set to 6m. The noise wall is established in the above bridge BEM model. To ensure the accuracy of noise prediction, the element size of the noise wall model is set to 0.2 m, and the wall surface is considered as rigid surface. The sound speed and density of air are 340 m/s and 1.225 kg/m^3, respectively. Taking the loaded containers condition as an example, the effect of the noise wall on the bridge radiated noise is investigated. To comprehensively evaluate the noise reduction effect of the noise wall, 12 typical field points (N1′~N12′) with heights of 2 m, 4 m, and 6 m above the ground and lateral distances of 1 m, 5 m, 10 m, and 15 m from the noise wall are selected, as shown in Figure 9.

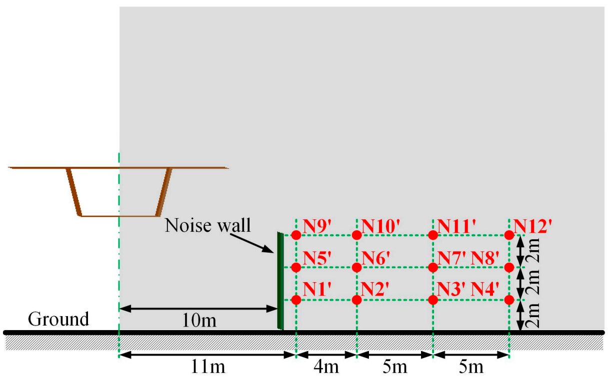

Figure 9. Layout of typical field points.

Figure 10 shows the comparison of SPLs at typical field points under conditions with or without the noise wall. It can be observed that the SPLs of all points are significantly reduced after setting the noise wall, and the closer the field point is to the ground and the noise wall, the better the overall noise reduction effect of the noise wall is. At field points N1′~N4′, the noise reduction effect of the noise wall is significant in the frequency ranges of 5~75 Hz and above 130 Hz. In the frequency range near the main frequency (60~90 Hz), the maximum reduction values of SPLs at each point are 24.6 dB, 28.6 dB, 33.1 dB, and 20.4 dB, respectively. For field points N5′~N8′, the noise wall has a great noise reduction effect in the frequency ranges below 35 Hz and above 140 Hz, and the maximum

SPL reduction values of each point near the main frequency are 23.3 dB, 20.8 dB, 14.9 dB, and 14.6 dB, respectively. Regarding field points N9′~N12′, the main action range of the noise wall is in the frequency range below 20 Hz and between 135 and 150 Hz, and the corresponding maximum reduction values of SPL in the main frequency range are 18.7 dB, 14.6 dB, 14.6 dB, and 28.8 dB, respectively.

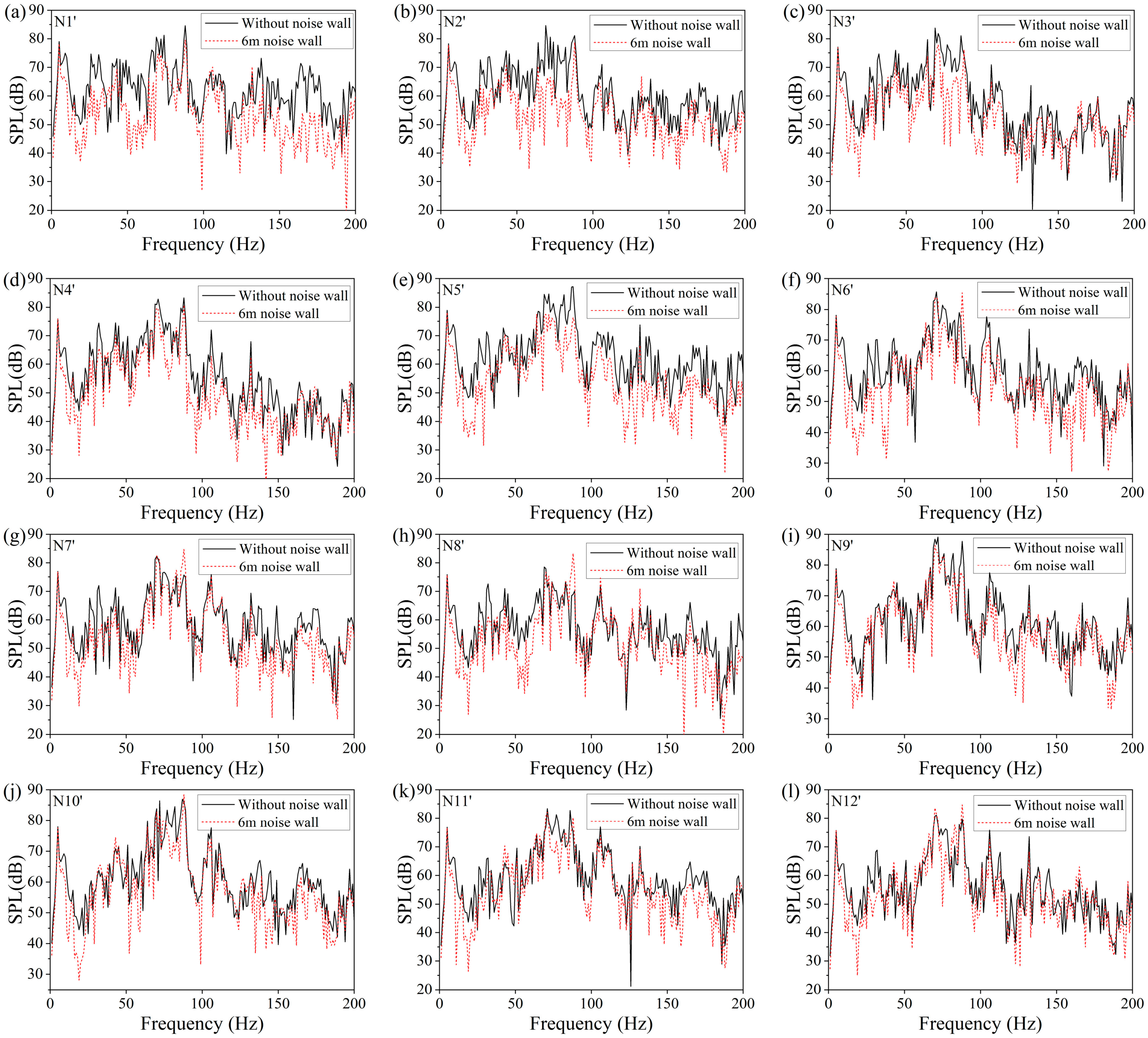

Figure 10. Comparisons of frequency-domain SPLs with/ without noise wall at filed points (**a**) N1′; (**b**) N2′; (**c**) N3′; (**d**) N4′; (**e**) N5′; (**f**) N6′; (**g**) N7′; (**h**) N8′; (**i**) N9′; (**j**) N10′; (**k**) N11′; and (**l**) N12′.

4.2. Influence of the Noise Wall Height

Based on the above analysis, the influence of the noise wall height on the noise reduction effect is further investigated, and the noise wall heights are set to be 4 m, 6 m, and 8 m. Figure 11 shows comparisons of 1/3 octave SPLs and insertion losses at six typical field points (N1′~N5′ and N9′). Moreover, the equal-loudness-level in "ISO 226 Acoustic—Normal equal-loudness-level Contours" [35] is introduced to evaluate the sensitivity of radiated noise in the human ear.

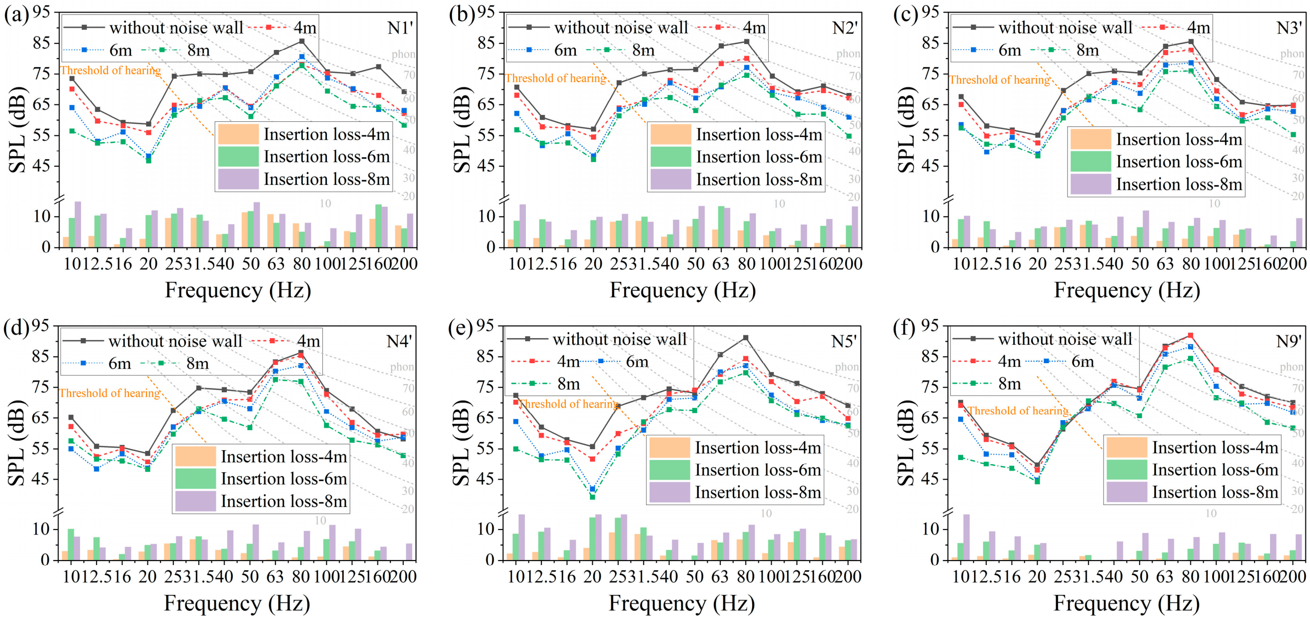

Figure 11. Comparisons of 1/3 octave band SPLs and insertion losses under different noise wall height conditions at field points (**a**) N1′; (**b**) N2′; (**c**) N3′; (**d**) N4′; (**e**) N5′; and (**f**) N9′.

In the frequency below 20 Hz, the noise reduction effect of the noise wall works significantly at all points under different noise wall height conditions, and the insertion loss overall increases with the noise wall height, among which the maximum insertion loss of 17.5 dB appears at field point N5′ in the frequency of 10 Hz. The SPLs at all points except point N9′ also decrease with the increase in the noise wall height after setting the noise wall in the frequency range of 20~31.5 Hz, but the overall noise reduction effect changes less with the wall height. The maximum insertion losses at points N1′~N4′ appear at 25 Hz, which are 12.7 dB, 10.8 dB, 9.0 dB, and 7.8 dB, respectively. For the field point N5′, the SPLs under conditions of 6m and 8 m noise walls are close, the noise reduction effect is significantly enhanced compared to the condition of 4 m noise wall, and the maximum insertion loss exceeds 16 dB. Similar to that in the frequency below 20 Hz, the SPLs of all points decrease with the noise wall height in the frequency range of 40 Hz and above, and all the maximum insertion losses appear in the frequency range of 50~80 Hz, among which all the maximum insertion losses of points N1′~N5′ all exceed 11 dB, and the maximum value of the point N9′ attains 9.0 dB. According to Refs. [20,36–39], the application of a vibration-damping fastener can reduce radiation noise by 0.5~2.8 dB, and the noise reduction effect of elastomer mats is about 8~23 dB. The above analysis indicates that the noise reduction range of the noise wall at typical points is between 8 and 17.5 dB, which is close to that of structural vibration reduction measures.

From the perspective of loudness level, the SPLs of typical field points under noise wall conditions are below the threshold of hearing at the frequency of 25 Hz and below. In the frequency range between 31.5 Hz and 80 Hz, the loudness levels of field points significantly increase with frequency, and the maximum value exceeds 70 phon. In the frequency range above 80 Hz, the loudness levels fluctuate slightly with the frequency within 40~60 phon. Compared with that under the without noise wall condition, the loudness levels under 6 m and 8 m noise wall conditions are significantly reduced in the frequency range of 31.5~80 Hz, and the maximum reduction attains 20 phon at 50 Hz, while the reductions of loudness levels under the 4 m noise wall condition are within 10 phon.

To demonstrate the noise reduction effect of the noise wall in the whole sound field, the insertion loss distributions at peak frequencies of the acoustic power, namely 9 Hz, 71 Hz, and 82 Hz, are shown in Figure 12. It can be seen that the insertion loss at the area behind the noise wall and below the deck is overall positive, which represents the noise reduction area, and the others are the noise increase area. As shown in Figure 12a–c, the insertion losses of the noise reduction area at 9 Hz are small under the 4 m noise wall condition, with a maximum of 4 dB. The maximum insertion loss under the 6 m noise wall condition is about 12 dB located at the area 15~20 m behind the noise wall. For the condition of an 8 m noise wall, the insertion loss decreases with the increase in distance from the noise wall, and the maximum insertion loss is about 18 dB. The SPLs outside the noise reduction area are generally increased small, within 8 dB. At the frequency of 71 Hz, the maximum insertion loss under the 4 m noise wall condition is located at the area about 1 m behind the wall with a maximum of 25 dB, while the noise reduction area under 6 m and 8 m noise wall conditions emerges zonal distributions, and the maximum values are 16 dB and 55 dB, respectively, but the noise of the area in front of the noise wall increases significantly with maximum increases of 21 dB and 25 dB, respectively, as shown in Figure 12d–f. It can be seen from Figure 12g–i that the noise reduction and increase areas are approximately divided by the noise wall plane at 82 Hz. The maximum noise reduction and increase values are located at different positions under different noise wall height conditions, but the maximum values are close, attaining 46 dB and 26 dB, respectively.

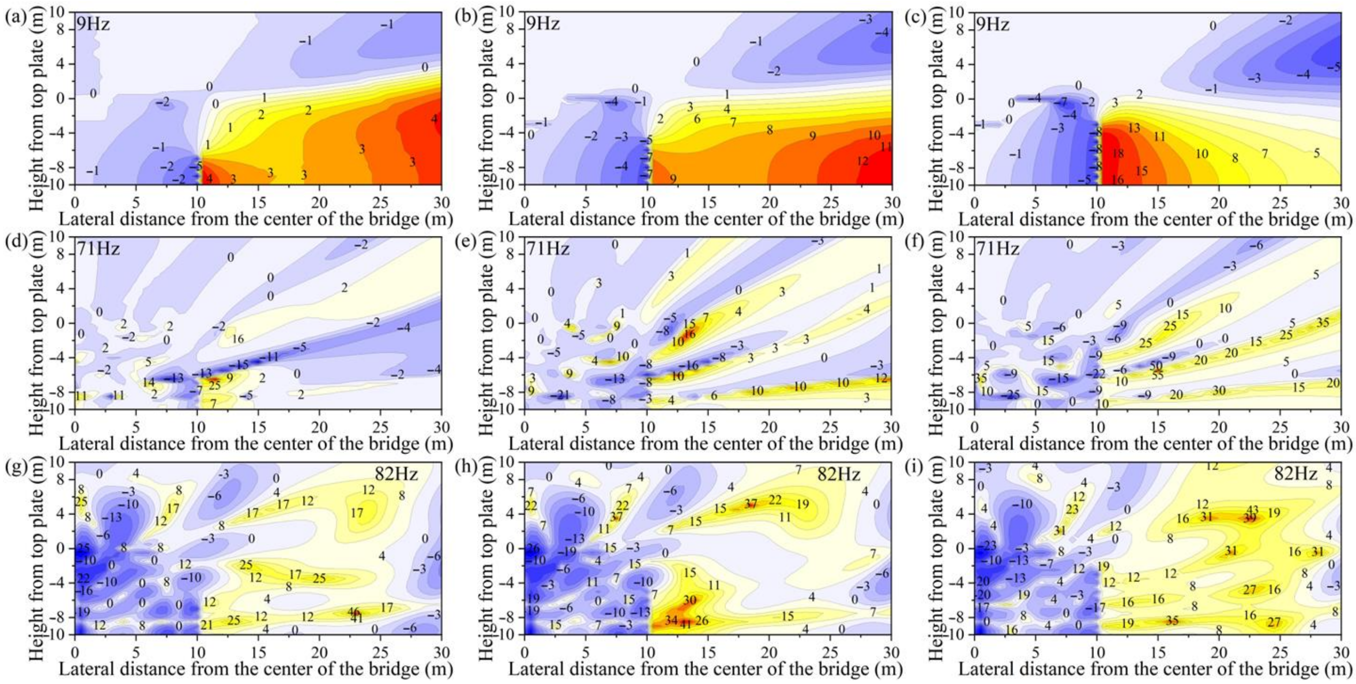

Figure 12. Insertion losses distributions under the noise wall heights of (**a**) 4 m, (**b**) 6 m, and (**c**) 8 m at 9 Hz; (**d**) 4 m, (**e**) 6 m, and (**f**) 8 m at 71 Hz; (**g**) 4 m, (**h**) 6 m, and (**i**) 8 m at 82 Hz.

For the scenario analyzed above, the ground reflection is considered, and the noise at each point in the sound field is mainly composed of the direct radiation part from the sound source and the superposition part of the ground-reflected sound waves. After setting the noise wall, there are three transmission paths for the radiated noise at the noise wall interface: reflection, diffraction, and transmission. The reflection path mainly affects the noise in the area below the bridge, causing increases in SPLs. The diffraction and transmission paths mainly affect the area behind the noise wall, and the sound waves are attenuated after transmitting the noise wall, resulting in a great noise reduction effect of the sound shadow zone. The diffracted and transmitted sound waves further influence the noise superposition results in other areas through ground reflection, causing changes in the SPL distribution outside the sound shadow zone.

5. Conclusions

In this study, we focus on the bridge-borne noise induced by the freight EMU with the speed of 350 km/h, we study the mechanism of bridge-borne noise is, and the noise reduction effect of the noise wall is further investigated. The characteristics of the bridge-borne noise under different loading conditions are analyzed, and the mechanism of radiation noise is revealed. Moreover, the effects of setting noise walls on bridge radiation noise are studied, and the influences of the noise wall height are investigated. The main conclusions are as follows:

(1) Compared with the condition of the empty containers, the accelerations of the bridge deck increase slightly under the loaded condition. Correspondingly, the bridge sound power and SPLs have a small increase in the frequency range below 20 Hz and above 125 Hz, and the maximum increments of the sound power and SPLs are 6.8 dB and 2.5 dB, respectively.
(2) The structure resonance, intense local vibrations, and high acoustic radiation efficiency of the bridge are related to the strong bridge radiation noise. The vibration of the deck is dominant, and the modes of the deck are conformed to the surface mode when the structural vibration frequency is greater than the critical frequency, which leads to high acoustic radiation efficiency.
(3) The bridge radiation noise is attenuated when transmitting the noise wall, resulting in a good noise reduction effect in the sound shadow zone, but the noise in local areas between the bridge and the noise wall increases due to the sound wave reflection of the noise wall. The ground reflection affects the superposition of transmitted, reflected, and diffracted sound waves, which causes nonlinear relationships of noise reduction effects with the noise wall height.
(4) The loudness levels of typical field points increase with frequency in the range of 20~80 Hz, while they fluctuate slightly within 40~60 phon in the frequency range above 80 Hz. Compared to the condition without the noise wall, the reductions of loudness level are within 10 phon under the 4 m noise wall condition, and the maximum reductions under 6 m and 8 m noise wall conditions attain 20 phon.

This paper only presents a simple simulation case of noise walls; full-scale or reduction-scale experiments should considered for further investigation when conditions permit them to be carried out. Moreover, future research should emphasize sound-absorbing materials to achieve better noise reduction effects.

Author Contributions: Conceptualization, M.D. and X.Z.; methodology, X.Z.; software, M.D.; validation, M.D. and X.Z.; formal analysis, M.D. and X.G.; investigation, M.D.; resources, K.W. and X.Z.; data curation, M.D.; writing—original draft preparation, M.D.; writing—review and editing, X.G., K.W. and X.Z.; visualization, M.D. and X.G.; supervision, K.W. and X.Z.; project administration, K.W. and X.Z.; funding acquisition, K.W. and X.Z. All authors have read and agreed to the published version of the manuscript.

Funding: This research was funded by Wang, K. and Zhang, X. The grant numbers are U19A20110, 52362049, 22JR5RA344, 22JR11RA152, 22ZY1QA005 and LZJTU-ZDYF2302. And APC was funded by U19A20110.

Institutional Review Board Statement: Not applicable.

Informed Consent Statement: Not applicable.

Data Availability Statement: Data is contained within the article.

Conflicts of Interest: Author Xin Ge was employed by the company CRRC Qingdao Sifang Co., Ltd. The remaining authors declare that the research was conducted in the absence of any commercial or financial relationships that could be construed as a potential conflict of interest.

References

1. The operating mileage of China's high-speed rail has reached 45000 km. *Railw. Tech. Superv.* **2024**, *52*, 38.
2. Shao, Z.; Bai, W.; Dai, J.; Yu, H.; Tong, Y. Monitoring and analysis of railway-induced vibration and structure-borne noise in a transit oriented development project. *Structures* **2023**, *57*, 105097. [CrossRef]
3. Moritoh, Y.; Zenda, Y.; Nagakura, K. Noise control of high speed Shinkansen. *J. Sound Vib.* **1996**, *193*, 319–334. [CrossRef]

4. Ngai, K.W.; Ng, C.F. Structure-borne noise and vibration of concrete box structure and rail viaduct. *J. Sound Vib.* **2002**, *255*, 281–297. [CrossRef]
5. Poisson, F.; Margiocchi, F. The use of dynamic dampers on the rail to reduce the noise of steel railway bridges. *J. Sound Vib.* **2006**, *293*, 944–952. [CrossRef]
6. Liang, L.; Li, X.; Sun, Y.; Gong, Z.; Bi, R. Measurement research on vibro-acoustic characteristics of large-span plate-truss composite bridge in urban rail transit. *Appl. Acoust.* **2022**, *187*, 108518. [CrossRef]
7. Zhang, X.; Zhai, W.; Chen, Z.; Yang, J. Characteristic and mechanism of structural acoustic radiation for box girder bridge in urban rail transit. *Sci. Total Environ.* **2018**, *627*, 1303–1314. [CrossRef]
8. Zhang, X.; Zhang, X.; Yang, J.; Zhu, S.; He, Q. Mechanism of noise reduction caused by thickening top plate for high-speed railway box-girder bridge. *Structures* **2023**, *57*, 105148. [CrossRef]
9. Li, X.; Liu, Q.; Pei, S.; Song, L.; Zhang, X. Structure-borne noise of railway composite bridge: Numerical simulation and experimental validation. *J. Sound Vib.* **2015**, *353*, 378–394. [CrossRef]
10. Li, Q.; Xu, Y.L.; Wu, D.J. Concrete bridge-borne low-frequency noise simulation based on train–track–bridge dynamic interaction. *J. Sound Vib.* **2012**, *331*, 2457–2470. [CrossRef]
11. Li, Q.; Song, X.; Wu, D. A 2.5-dimensional method for the prediction of structure-borne low-frequency noise from concrete rail transit bridges. *J. Acoust. Soc. Am.* **2014**, *135*, 2718–2726. [CrossRef]
12. Song, X.D.; Wu, D.J.; Li, Q.; Botteldooren, D. Structure-borne low-frequency noise from multi-span bridges: A prediction method and spatial distribution. *J. Sound Vib.* **2016**, *367*, 114–128. [CrossRef]
13. Wu, T.; Liu, J. Sound emission comparisons between the box-section and U-section concrete viaducts for elevated railway. *Noise Control Eng. J.* **2012**, *60*, 450–457. [CrossRef]
14. Liu, X.; Zhang, N.; Sun, Q.; Wang, Z.; Zhang, C. An efficient frequency domain analysis method for bridge structure-borne noise prediction under train load and its application in noise reduction. *Appl. Acoust.* **2022**, *192*, 108647. [CrossRef]
15. Zbiciak, A.; Kraśkiewicz, C.; Dudziak, S.; Al-Sabouni-Zawadzka, A.; Pełczyński, J. An accurate method for fast assessment of under slab mats (USM) performance in ballastless track structures. *Constr. Build. Mater.* **2021**, *300*, 123953. [CrossRef]
16. Kraśkiewicz, C.; Zbiciak, A.; Pełczyński, J.; Al Sabouni-Zawadzka, A. Experimental and numerical testing of prototypical under ballast mats (UBMs) produced from deconstructed tires—The effect of mat thickness. *Constr. Build. Mater.* **2023**, *369*, 130559. [CrossRef]
17. Wettschureck, G.; Heim, M.; Tecklenburg, M. Long-term properties of Sylomer® ballast mats installed in the rapid transit railway tunnel near the Philharmonic Hall of Munich, Germany. *Rail Eng. Int.* **2002**, *31*, 6–11.
18. Züblin, A.G. Installation of highly effective vibration mitigation measures in a railway tunnel in Cologne, Germany. *Rail Eng. Int.* **1999**, *4*, 12–16.
19. Ahac, M.; Haladin, I. Experimental investigation of railway track with under sleeper pad. In Proceedings of the 10th Slovenian Road and Transportation Congress, Portoroz, Slovenia, 20–22 October 2010.
20. Liang, L.; Li, X.; Zheng, J.; Lei, K.; Gou, H. Structure-borne noise from long-span steel truss cable-stayed bridge under damping pad floating slab: Experimental and numerical analysis. *Appl. Acoust.* **2020**, *157*, 106988. [CrossRef]
21. Li, Q.; Dai, B.; Zhu, Z.; Thompson, D.J. Comparison of vibration and noise characteristics of urban rail transit bridges with box-girder and U-shaped sections. *Appl. Acoust.* **2022**, *186*, 108494. [CrossRef]
22. Harrison, M.F.; Thompson, D.J.; Jones, C.J.C. The calculation of noise from railway viaducts and bridges. *Proc. Inst. Mech. Eng. Part F J. Rail Rapid Transit* **2000**, *214*, 125–134. [CrossRef]
23. Zhang, X.; Li, X.; Li, X.; Liu, Q.; Zhang, Z. Train-induced vibration and noise radiation of a prestressed concrete box-girder. *Noise Control Eng. J.* **2013**, *61*, 425–435. [CrossRef]
24. Zhang, X.; Li, X.; Liu, Q.; Wu, J.; Li, Y. Theoretical and experimental investigation on bridge-borne noise under moving high-speed train. *Sci. China Technol. Sci.* **2013**, *56*, 917–924. [CrossRef]
25. Zhai, W. *Vehicle-Track Coupled Dynamics: Theory and Applications*; Springer: Singapore, 2020.
26. Kalker, J.J. A fast algorithm for the simplified theory of rolling contact. *Veh. Syst. Dyn.* **1982**, *11*, 1–13. [CrossRef]
27. Jiang, W.; Wu, H. *Acoustic Boundary Element Method and Its Fast Algorithm*; Science Press: Beijing, China, 2019.
28. Thompson, D.J. *Railway Noise and Vibration: Mechanisms, Modelling and Means of Control*; Elsevier: Amsterdam, The Netherlands, 2008.
29. Zhang, X.; Li, X.; Hao, H.; Wang, D.; Li, Y. A case study of interior low-frequency noise from box-shaped bridge girders induced by running trains: Its mechanism, prediction and countermeasures. *J. Sound Vib.* **2016**, *367*, 129–144. [CrossRef]
30. Liu, L.; Xu, D. Structural noise radiation characteristics of box beams with web holes. *Shock Vib.* **2016**, *35*, 204–210.
31. Li, X.; Zhang, X.; Zhang, Z.; Liu, Q.; Li, Y. Experimental research on noise emanating from concrete box-girder bridges on intercity railway lines. *Proc. Inst. Mech. Eng. Part F J. Rail Rapid Transit* **2015**, *229*, 125–135. [CrossRef]
32. He, L.; Zhu, H.C.; Qiu, X.J.; Du, G.H. *Acoustic Theory and Engineering Applications*; Science Press: Beijing, China, 2006.
33. Dai, R. Analysis on acoustic radiation characteristics at coincidence frequency of rectangular Plate. *J. Sichuan Ordnance Eng.* **2014**, *35*, 143–145.
34. Zhang, T.; Liu, Y.; Luo, Y.; Zhou, L. Research on the influence of ground acoustic wall height on elevated structure noise of rail transit. *J. Railw. Sci. Eng.* **2019**, *16*, 168–175.
35. *ISO 226:2003*; Acoustics—Normal Equal-Loudness-Level Contours. International Standardization Organization: Geneva, Switzerland, 2003.

36. Wang, P.; Tang, J.; Yang, P. Analysis of the influence of GJ-III fastener vibration damping track on environment noise of metro viaduct section. *Railw. Stand. Des.* **2017**, *61*, 4–9. (In Chinese)
37. Song, X.; Li, Q. Numerical and experimental study on noise reduction of concrete LRT bridges. *Sci. Total Environ.* **2018**, *643*, 208–224. [CrossRef]
38. Zhang, X.; Cao, Z.; Ruan, L.; Li, X.; Li, X. Reduction of vibration and noise in rail transit steel bridges using elastomer mats: Numerical analysis and experimental validation. *Proc. Inst. Mech. Eng. Part F J. Rail Rapid Transit* **2021**, *235*, 248–261. [CrossRef]
39. Liu, L.; Song, R.; Zhou, Y.L.; Qin, J. Noise and vibration mitigation performance of damping pad under CRTS-III ballastless track in high speed rail viaduct. *KSCE J. Civ. Eng.* **2019**, *23*, 3525–3534. [CrossRef]